


 Cite this: *RSC Adv.*, 2021, **11**, 36636

## Nanoarchitectonics of p-type BiSbTe with improved figure of merit *via* introducing PbTe nanoparticles†

 Yuanyue Li, Mengna Ren, Zhongsen Sun\* and Zhao Yao \*

$\text{Bi}_{0.4}\text{Sb}_{1.6}\text{Te}_3$  (BST) is known to be a unique p-type commercial thermoelectric (TE) alloy used at room temperatures, but its figure of merit ( $ZT$ ) is relatively low for wide industrial applications. To improve its  $ZT$  value is vitally important. Here, we show that the incorporation of 0.5 wt% PbTe nanoparticles into BST concurrently causes a large enhancement of power factor (PF) and a significant reduction of lattice thermal conductivity  $\kappa_L$ . The increase in PF mainly benefits from the optimization of carrier concentration, maintenance of high carrier mobility and constant rise in Seebeck coefficient. The decrease in  $\kappa_L$  can be attributed to the enhanced phonon scattering by the dispersed PbTe nanoparticles and the interfaces between PbTe and the BST matrix by using the Callaway model. Specifically, an ultralow  $\kappa_L$  of  $0.26 \text{ W m}^{-1} \text{ K}^{-1}$  at  $429 \text{ K}$  is achieved for the composites incorporating 0.5 wt% PbTe nanoinclusions. Consequently, an excellent  $ZT = 1.6$  at  $482 \text{ K}$  and a high average  $ZT_{\text{ave}} = 1.38$  at  $300\text{--}500 \text{ K}$  are achieved, indicating that incorporation of PbTe in BST is an effective approach to improve its thermoelectric performance.

Received 24th September 2021

Accepted 6th November 2021

DOI: 10.1039/d1ra07138f

[rsc.li/rsc-advances](http://rsc.li/rsc-advances)

### 1. Introduction

Thermoelectric (TE) materials have attracted much attention as clean renewable sources because of their capability to harvest energy.<sup>1–3</sup> The efficiency of TE materials is determined by the dimensionless figure of merit ( $ZT$ ), defined as  $ZT = S^2 T / \rho \kappa$ , where  $T$ ,  $S$ ,  $\rho$  and  $\kappa$  are the absolute temperature, Seebeck coefficient, electrical resistivity and thermal conductivity, respectively.<sup>4,5</sup> In order to achieve high  $ZT$  values, one must maximize the power factor PF ( $= S^2 / \rho$ ) and simultaneously minimize the thermal conductivity  $\kappa$ . However,  $S$ ,  $\rho$  and  $\kappa$  are dependent on each other, and it is extremely difficult to simultaneously optimize these three TE parameters.

$\text{BiSbTe}$  is the best known p-type TE material at room temperatures. Over the years, various strategies have been implemented to elevate the  $ZT$  values of  $\text{BiSbTe}$  alloys. Among them, optimizing the hole concentration  $p$  is the most effective way to improve the electrical transport and achieve high PF.<sup>6,7</sup> In p-type  $\text{BiSbTe}$  crystal, when cations occupy the vacant anion sites, it creates antisite defects. The formation energy of antisite defects depends on polarity of the bonds between cations and anions. The hole concentration  $p$  can be increased by raising the Sb content in  $\text{BiSbTe}$  structure as it can reduce the formation energy of antisite defects. Previous studies have shown that

$\text{Bi}_{0.4}\text{Sb}_{1.6}\text{Te}_3$  (BST) possesses the optimal  $p$  ( $\sim 10^{19} \text{ cm}^{-3}$ ) and the highest PF ( $\sim 45 \mu\text{W cm}^{-1} \text{ K}^{-2}$ ) at room temperature.<sup>8–11</sup> On the other hand, nanostructuring and nanocompositing in bulk materials have been widely employed to intensify the scattering of phonons in order to reduce  $\kappa$ .<sup>12–15</sup> Compared to TE nanomaterials, nanocomposite TE materials are relatively easy to prepare and investigate. The introduction of nanoinclusions into bulk TE materials can simultaneously create a high density of phase boundaries to scatter phonons in order to greatly lower  $\kappa$ . However, in this case PF generally declines due to sharp reduction in carrier mobility  $\mu$ . Therefore, whether one can introduce nanoinclusions into BST alloys that can not only reduce  $\kappa$  but also enhance PF is greatly challenging, because this will bring a large improvement of  $ZT$ .

In this work, BST alloys containing PbTe nanoparticles were fabricated, and their TE properties were investigated. PbTe is one of the most studied TE materials with a high  $ZT$  value of 1.8–2.2 at medium temperatures.<sup>16,17</sup> Several previous reports have been reported about the TE properties of the composite with bismuth telluride and PbTe,<sup>18,19</sup> but their  $ZT$  values are still relatively low for wide applications. In our experiment, PbTe nanoparticles were synthesized through hydrothermal procedure, which is different from the previously reported vacuum melting method.<sup>18,19</sup> In this way, the obtained PbTe nanoparticles own the advantages of small granularity, uniform distribution and less reunion, which will effectively enhance phonon scattering and reduce the lattice thermal conductivity  $\kappa_L$  in the PbTe/BST nanocomposites. In addition, the asymmetric interface potentials between PbTe and BST will inhibit

College of Electronic and Information Engineering, Qingdao University, Qingdao 266071, China. E-mail: sunzs@qdu.edu.cn; yao9074@hotmail.com

† Electronic supplementary information (ESI) available. See DOI: 10.1039/d1ra07138f



the transport of the thermally excited electrons to lower the bipolar effect, which will elevate  $S$  and reduce  $\kappa$  at elevated temperatures. Our experimental results show that the incorporation of 0.5 wt% of PbTe into BST indeed results in both enhanced PF and reduced  $\kappa$ . Specifically, an extremely low  $\kappa_L$  of  $0.26 \text{ W m}^{-1} \text{ K}^{-1}$  at 429 K is reached, approaching the amorphous limit in the BiSbTe system, while maintaining a high PF. Consequently, a peak  $ZT$  of 1.6 at 482 K and a high average  $ZT$  ( $ZT_{ave}$ ) of 1.38 at 300–500 K are achieved in the nanocomposites with 0.5 wt% PbTe, which are comparable to other reported start-of-the-art TE materials in the same range of temperature.<sup>12,16,20–25</sup> In what follows, the effect of the incorporation of PbTe nanoparticles on the TE properties of BST alloys will be analyzed in details.

## 2. Experimental

As shown in Fig. 1, elemental powders Bi (99.99%, Alfa Aesar), Sb (99.9%, Sigma Aldrich), and Te (99.99%, Alfa Aesar) granules were weighted according to the formula of  $\text{Bi}_{0.4}\text{Sb}_{1.6}\text{Te}_3$  doped with 3 wt% Te. The powder mixture was loaded into quartz ampoule sealed under vacuum at  $10^{-3}$  Pa, and heated to 1073 K for 10 h. Then the ingot was grinded into powders. To synthesize the lead telluride with the nominal composition, 5 g  $\text{NaBH}_4$  and 15 g  $\text{NaOH}$  were put into a glass beaker filled with 600 mL deionized water; then 200 mL anhydrous ethylenediamine was added to the beaker. To make the reaction proceed homogeneously, the solution was stirred at room temperature with a magnetic stirrer. In the process, 50 mmol Te powder was added into the solution. Then, the solution was heated to 423 K on the oil bath. Subsequently, 50 mmol  $\text{PbCl}_2$  was added in the beaker; then, the solution was stirred at a speed of 1700 rpm and was kept at 423 K. After about 1 h, a large quantity of powders were precipitated. Then the precipitates were collected, filtered and washed respectively with anhydrous ethanol and distilled water until a pH value close to 7. The acquired powders

were then dried in vacuum furnace at 353 K for 6 h. The nanometer-sized PbTe and BST powders were mixed in a planetary mill for 2 h with a certain weight ratios of 0.25 : 99.75, 0.5 : 99.5, 1 : 99. Then the bulk nanocomposite samples were obtained by hot-pressing the blended powders under a pressure of 600 MPa in a vacuum at 673 K for 1 h.

The phase structure of sample was studied by X-ray diffraction (XRD, Philips diffractometer,  $\text{Cu K}\alpha$  radiation) at room temperature. The fractograph of the composite  $\chi(\text{PbTe})/\text{BST}$  (here, we take  $\chi = 0.5$  wt% for instance) was observed by field emission scanning electron microscopy (FE-SEM, FEI Sirion 200). Moreover, transmission electron microscopy (TEM, Tecnai F30) was used to carry out the microstructure investigations. X-ray photoelectron spectroscopy (XPS, Thermo Kalpha) was used to perform element analysis of the composite sample.  $\rho$  and  $S$  were measured simultaneously by commercial equipment (ULVAC-RIKO: ZEM-3, Japan) under He atmosphere from 300 to 500 K. The thermal diffusivity,  $D$ , was measured using the laser flash method (Netzsch, LFA-457). Moreover, in consideration of the anisotropic characteristic of  $\text{Bi}_2\text{Te}_3$ -based alloys,  $D$  was measured along the direction perpendicular to the hot-pressing direction, ensuring that the thermal and electrical properties were measured in the same direction. The specific heat,  $C_p$ , was determined by a commercial instrument (Pyris Diamond DSC, PerkinElmer). The density,  $d$ , was measured by the Archimedes' method (using ethylalcohol as liquid medium, AR). The resulting total thermal conductivity  $\kappa$  was calculated from the measured thermal diffusivity  $D$ , density  $d$  and specific heat  $C_p$  from the relationship  $\kappa = DdC_p$ . The Hall coefficient was measured at 300 K using the physical property measurement system (PPMS), and the hole concentration  $p$  and mobility  $\mu$  were calculated using Hall coefficient and electrical resistivity  $\rho$ . The accuracies in  $\rho$ ,  $S$ , and  $\kappa$  are around  $\pm 2$ ,  $\pm 3$ , and  $\pm 5\%$ , respectively. The combined uncertainty of  $ZT$  is around  $\pm 12\%$ .

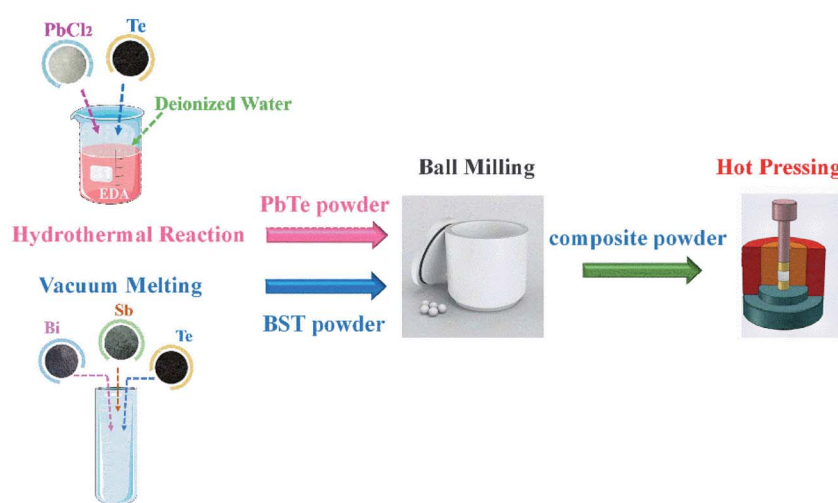


Fig. 1 Schematic diagram of the hydrothermal reaction for PbTe powder, vacuum melting for BST samples, ball milling and hot pressing processes.



### 3. Results and discussion

Fig. 2(a) shows XRD patterns of BST, PbTe and composite samples  $\chi$ (PbTe)/BST ( $\chi = 0.25, 0.5$  and  $1.0$  wt%). The main diffraction peaks correspond well to the standard JCPDS cards (BST: no. 72-1836, PbTe: no. 002-1132). Apart from the main diffraction peaks of BST, an additional small peak (200) from the PbTe phase appears in the XRD patterns of the composite samples ( $\chi > 0$ ), and the intensity of the peak increases with the increasing PbTe content, which indicates that no obvious impurity phase forms other than the two constituent phases (BST and PbTe). In addition, the average grain size for PbTe nanoparticles is  $\sim 30$  nm that is determined from peak broadening of the XRD pattern for PbTe based on the Scherrer formula.

The FESEM fractograph of the bulk PbTe/BST composite sample is shown in Fig. 2(b). The plate-shaped grains can be observed, which reveal the typical structure of BiSbTe-based compounds. By further careful inspection from Fig. 2(b), one can find some small particles with sizes of  $\sim 20$  to  $\sim 80$  nm distributed in the BST matrix (Fig. 2(c)). Further analysis with energy dispersive X-ray spectroscopy (EDX) indicates that the composites contain chemical element Pb and Te (Fig. S1†), verifying that the small particles are actually PbTe grains. The TEM image of PbTe/BST composite sample is shown in Fig. 2(d), from which one can see the PbTe nanoparticles, BST matrix and

typical phase boundaries between them (as shown by the white dash line). Furthermore, due to the difference of the band gaps of PbTe ( $E_g = 0.32$  eV) and BST ( $E_g = 0.17$  eV), p-p type interface potentials will form at the heterojunction interfaces to guarantee the equal chemical potentials on both sides,<sup>18,26,27</sup> as shown in Fig. S2.† In order to further examine chemical elements for the composite sample, XPS test was employed, and the overall spectrum is shown in Fig. 3. Fig. 3(a) discloses that the sample is composed of bismuth, tellurium, antimony and lead. Fig. 3(b)–(e) show the peaks corresponding to the bonding energies of Bi4f, Sb3d, Te3d and Pb4f, respectively. The XPS results clearly reveal that the composite sample contains two compounds: BST and PbTe.

The electrical resistivity  $\rho$  as a function of temperature of  $\chi$ (PbTe)/BST ( $\chi = 0, 0.25, 0.5$  and  $1.0$  wt%) is shown in Fig. 4(a). One can see that  $\rho$  for all the samples increases with increasing temperature, exhibiting a degenerate semiconductor behavior. On the other hand,  $\rho$  decreases with increasing content of PbTe. For example,  $\rho$  at 300 K decreases from 0.746 to 0.647, 0.448 and 0.381  $\Omega$  m, as  $\chi$  increases from 0 to 0.25, 0.5 and 1.0 wt%, respectively. As shown in Fig. 4(b), the positive values of  $S$  for the composite samples ( $\chi > 0$ ) means that the major carriers in all the samples are holes.  $S$  decreases obviously with increasing content of PbTe. An interesting phenomenon, which can also be found in our previous work,<sup>18,26,27</sup> is that the temperature at which  $S$  reach a maximum shifts to higher temperature as  $\chi$

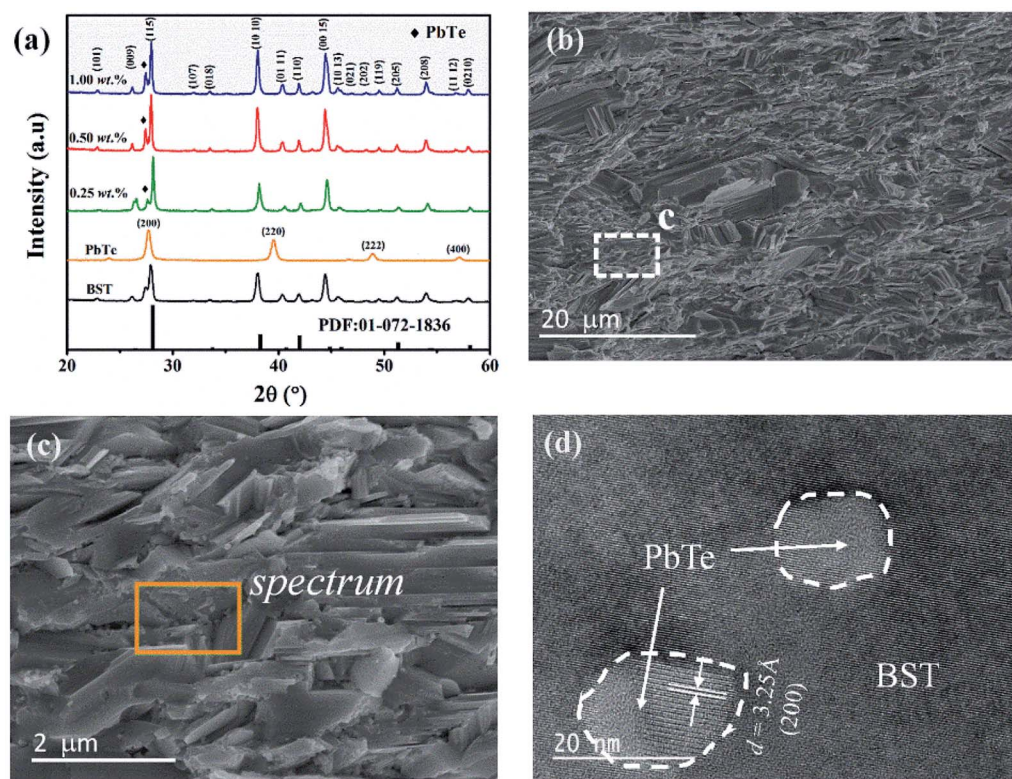


Fig. 2 (a) XRD patterns for BST, PbTe and composite samples  $\chi$ (PbTe)/BST ( $\chi = 0.25, 0.5$  and  $1.0$  wt%); (b) FE-SEM micrograph of fracture surface of PbTe/BST bulk composite sample; (c) HRSEM image of the selected rectangle area in (b); (d) TEM bright-field image of PbTe/BST, showing the BST matrix, the incorporated PbTe nanoparticles and typical phase boundaries between them.



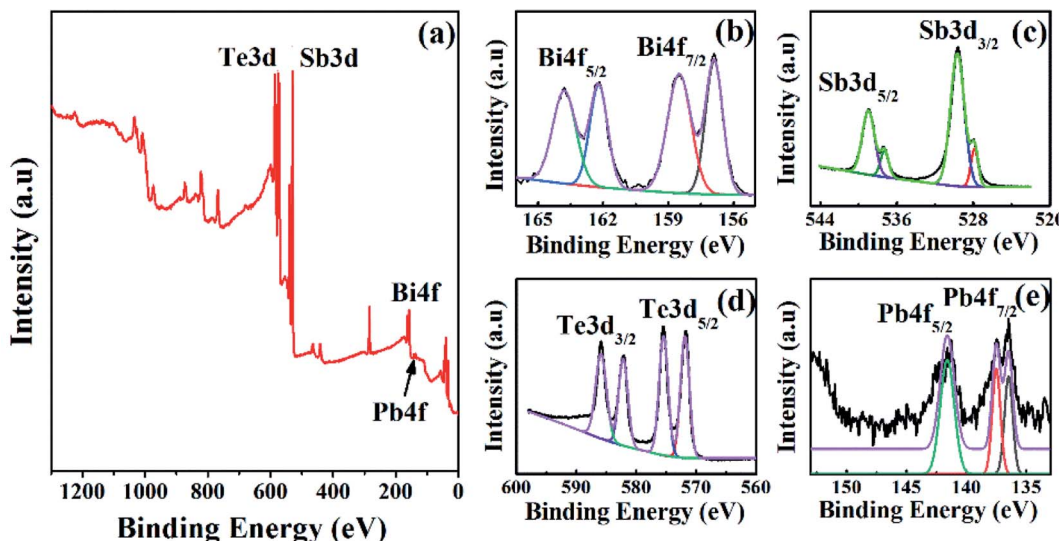


Fig. 3 XPS spectrum of PbTe/BST composite sample (a) survey spectrum; (b) Bi4f; (c) Sb3d; (d) Te3d; (e) Pb4f.

increases from 0 to 0.25, 0.5 and 1 wt%, and there is nearly no decline of  $S$  for the sample with  $\chi = 0.5$  and 1 wt%. The decline of  $S$  at high temperatures is due to the thermal excitation of electrons; however, the incorporation of PbTe nanoparticles can effectively inhibit the transport of these electrons by the interface potentials, and the more the PbTe content, the stronger

this inhibition effect. In addition, the band gap  $E_g$  of the BST can be roughly calculated to be 0.17 eV by using the Goldsmid-Sharp relationship  $E_g = 2eS_{\max}T_{\max}$ , where  $S_{\max}$  is the peak value of  $S$  and  $T_{\max}$  is the corresponding temperature.<sup>28</sup>

In order to understand the behavior of  $\rho$  and  $S$ , the hole concentration  $p$  was measured at room temperature. As shown

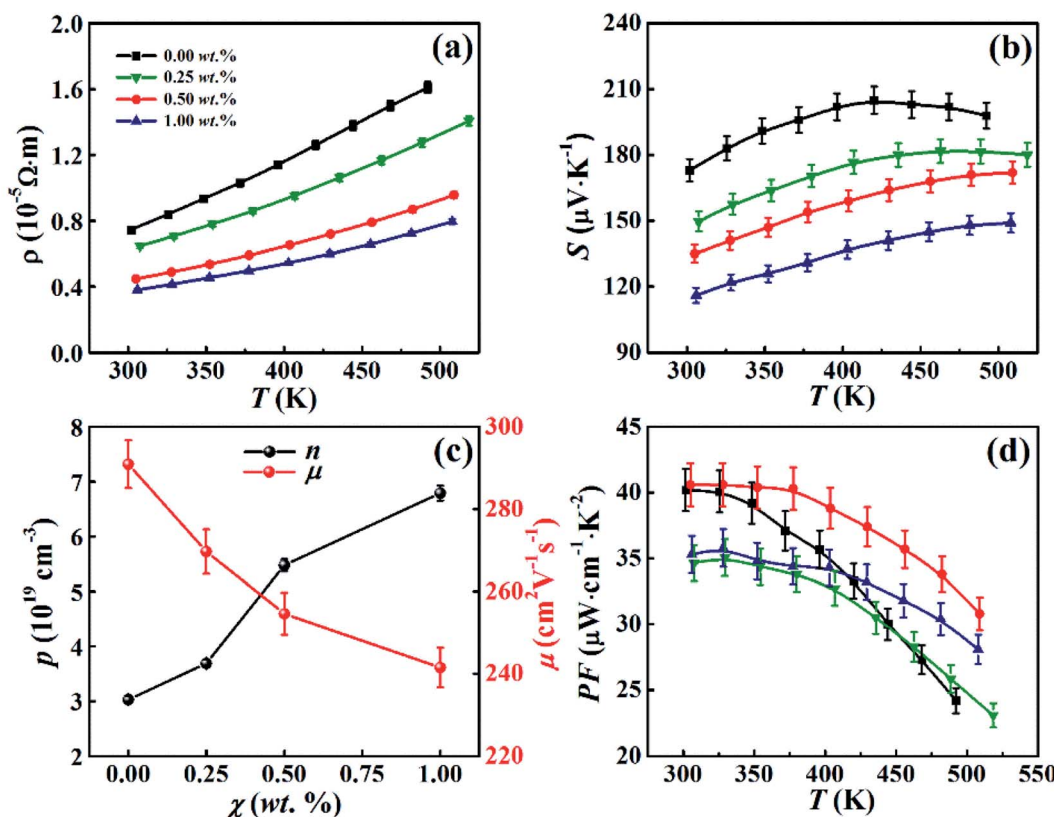


Fig. 4 Temperature dependences of (a) electrical resistivity  $\rho$ , (b) Seebeck coefficient  $S$  and (d) power factor  $PF$  for composite samples  $\chi$ (PbTe)/BST ( $\chi = 0, 0.25, 0.5$  and  $1$  wt%). (c) Varieties of hole concentration  $p$  and mobility  $\mu$  with PbTe content  $\chi$  for composite samples  $\chi$ (PbTe)/BST ( $\chi = 0, 0.25, 0.5$  and  $1$  wt%) at  $300$  K.

in Fig. 4(c),  $p$  increases from  $3.03 \times 10^{19}$  to  $6.79 \times 10^{19} \text{ cm}^{-3}$ , as  $\chi$  increases from 0 to 1 wt%. Meanwhile, the hole mobility  $\mu$  decreases from 290.9 to  $241.5 \text{ cm}^2 \text{ V}^{-1} \text{ s}^{-1}$  just with a small range according to the relationship  $\rho = 1/(p\mu)$ . This could be ascribed to that the lattice of PbTe with face-centered cubic structure can partly matching well with BST with dense hexagonal structure, which will weaken the carrier scattering to a certain extent. Furthermore,  $S$  of a degenerate semiconductor can be expressed by Mott formula:<sup>29</sup>

$$S = \frac{\pi^2 k_B^2 T}{3e} \left( \frac{\partial \ln(\sigma(E))}{\partial E} \right)_{E=E_f} = \frac{\pi^2 k_B^2 T}{3e} \left[ \frac{1}{p} \frac{\partial p(E)}{\partial E} + \frac{1}{\mu} \frac{\partial \mu(E)}{\partial E} \right]_{E=E_f} \quad (1)$$

Formula (1) indicates that  $S$  decreases with increasing  $p$ , which can be applied to explain qualitatively why  $S$  decreases with increasing PbTe nanoinclusions as shown in Fig. 4(b).

Fig. 4(d) shows PF of  $\chi(\text{PbTe})/\text{BST}$  ( $\chi = 0, 0.25, 0.5$  and  $1.0 \text{ wt\%}$ ) as functions of temperature. One can see that PF of the BST matrix decreases fast with increasing temperature, while PF of the composite samples ( $\chi > 0$ ) shows a relative slow descent speed. PF of the incorporated samples enhances obviously especially at elevated temperatures. Thereinto, PF of the sample with  $\chi = 0.5 \text{ wt\%}$  is larger than that of the BST matrix at the whole temperature range investigated here. For instance, PF of the sample with  $\chi = 0.5 \text{ wt\%}$  is  $33.8 \mu\text{W} (\text{cm}^{-1} \text{ K}^{-2})^{-1}$  at  $482 \text{ K}$ , which is  $\sim 33\%$  larger than that of the BST matrix ( $25.5 \mu\text{W} (\text{cm}^{-1} \text{ K}^{-2})^{-1}$ ).

The total thermal conductivity  $\kappa$  for all the samples is given in Fig. 5(a) as a function of temperature. One can see that  $\kappa$  for the BST matrix first decreases and then slightly increases with the elevation of temperature due to the bipolar effect. In comparison,  $\kappa$  for the composite samples ( $\chi > 0$ ) decreases with increasing temperature in the whole temperature range investigated, leading to a substantial decline in  $\kappa$  for the samples with  $\chi = 0.25$  and  $0.5 \text{ wt\%}$  especially at high temperatures. For instance, as to the sample with  $\chi = 0.5 \text{ wt\%}$ ,  $\kappa$  decreases from  $1.10$  to  $0.99 \mu\text{W} (\text{cm}^{-1} \text{ K}^{-2})^{-1}$  at  $482 \text{ K}$  (a  $\sim 10\%$  decline). The total thermal conductivity  $\kappa$  can be expressed as  $\kappa = \kappa_L + \kappa_C + \kappa_b$ , where  $\kappa_C$ ,  $\kappa_L$  and  $\kappa_b$  are the carrier thermal conductivity, lattice thermal conductivity, and thermal conductivity from the bipolar effect, respectively.<sup>30</sup> Among them,  $\kappa_C$  can be estimated by the Wiedemann-Franz relation ( $\kappa_C = LT/\rho$ ) as shown in Fig. 5(b), in which the Lorenz number  $L$  is estimated using formula (2) and (3) with the assumption of transport dominated by acoustic scattering and a single parabolic band:<sup>31</sup>

$$L = \left( \frac{k_B}{e} \right)^2 \frac{3F_0(\xi_F)F_2(\xi_F) - 4F_1(\xi_F)^2}{F_0(\xi_F)^2} \quad (2)$$

$$F_i(\xi_F) = \int_0^\infty \frac{x^i}{1 + e^{(x-\xi_F)}} dx \quad (3)$$

where  $\xi_F$  is the reduced Fermi level  $E_F/(k_B T)$ . The obtained values of  $L$  are  $1.46\text{--}1.59 \times 10^{-8} \text{ V}^2 \text{ K}^{-2}$ , as listed in Table S1.† Subsequently,  $\kappa_L + \kappa_b$  can be obtained from  $\kappa = LT/\rho$ , as shown

in Fig. 5(c). It can be seen that  $\kappa_L + \kappa_b$  for the BST matrix decreases first as the temperature increases from  $300$  to  $450 \text{ K}$ ; then, it increases as the temperature increases to  $500 \text{ K}$  due to a strong bipolar effect. By contrast,  $\kappa_L + \kappa_b$  for the composite samples ( $\chi > 0$ ) shows a slight increase as the temperature increases from  $450$  to  $500 \text{ K}$  due to a reduced bipolar effect, which can be ascribed to the inhibition of the transport of thermally excited electrons by the interface potentials between PbTe nanoinclusions and BST matrix.<sup>18,26,27</sup> Moreover,  $\kappa_L + \kappa_b$  for the composite samples ( $\chi > 0$ ) are reduced substantially as compared to that of the BST matrix. Specifically, a lower  $\kappa_L = 0.26 \text{ W m}^{-1} \text{ K}^{-1}$  at  $429 \text{ K}$  is reached for the sample with  $\chi = 0.5 \text{ wt\%}$ , which is smaller than these of the reported state-of-the-art p-type BiSbTe-based alloys.<sup>12,20-23</sup> In order to clarify why the composite samples ( $\chi > 0$ ) have significantly reduced  $\kappa_L$ , the Debye–Callaway model was adopted in which  $\kappa_L$  is expressed as:<sup>32</sup>

$$\kappa_L = \frac{4\pi k_B^4 T^3}{vh^3} \int_0^{\theta_D/T} \tau_T \frac{z^4 \exp(z)}{[\exp(z) - 1]^2} dz \quad (4)$$

where  $\theta_D$  is the Debye temperature,  $v$  is the average sound velocity,  $\tau_T$  is the total phonon relaxation time, and  $z$  is the reduced phonon frequency. In our composite samples ( $\chi > 0$ ), the dominant phonon-scattering mechanisms include scattering processes from point defects, incorporated PbTe nanoparticles, phonon–phonon Umklapp-scattering, and interfaces (grain/phase boundaries). Thus, total phonon relaxation time  $\tau_T$  can be expressed as the following relation:<sup>32</sup>

$$\frac{1}{\tau_T} = \frac{1}{\tau_{PD}} + \frac{1}{\tau_{NP}} + \frac{1}{\tau_U} + \frac{1}{\tau_E} + \frac{1}{\tau_{IF}} \quad (5)$$

where  $\tau_{PD}$ ,  $\tau_{NP}$ ,  $\tau_U$ ,  $\tau_E$  and  $\tau_{IF}$  are the relaxation times corresponding to scattering from the point defects, incorporated PbTe nanoparticles, phonon–phonon Umklapp-process, electron–phonon interaction and interfaces (between PbTe nano-phase and BST matrix), respectively. In the Rayleigh scattering regime, the scattering cross section  $\varphi$  has the relation  $\varphi \sim b^6 \omega^4$  (or  $\sim b^6/\lambda^4$ ), where  $b$  is the size of the scatters and  $\omega$  ( $\lambda$ ) is the phonon frequency (wavelength). In the BST matrix, point defects, such as impurities and alloy elements, are the domain point defects that have the size of  $b \sim 0.1 \text{ nm}$ , indicating that high-frequency (short-wavelength) phonons are scattered much more strongly than mid- and low-frequency (long-wavelength) phonons. Consequently, the mid- and low-frequency phonons are the main contributors to  $\kappa_L$  in BST. As the incorporated PbTe nanoparticles have sizes of  $\sim 20$  to  $\sim 80 \text{ nm}$  with mean value of  $\sim 30 \text{ nm}$ , the mid- and low-frequency phonons will be strongly scattered by the embedded PbTe nanoinclusions, leading to a sharp reduction of  $\kappa_L$ . Therefore, combining phonon scattering of both conventional point defects and embedded PbTe nanoparticles together because of their Rayleigh scattering character, formula (5) can be rewritten as<sup>32,33</sup>

$$\tau_T^{-1} = A\omega^4 + B\omega^2 T \exp(-\theta_D/3T) + C\omega^2 + v/l \quad (6)$$

where  $l$  is the mean spatial distance among the PbTe nanoparticles in the BST matrix, and the term  $v/l$  represents the



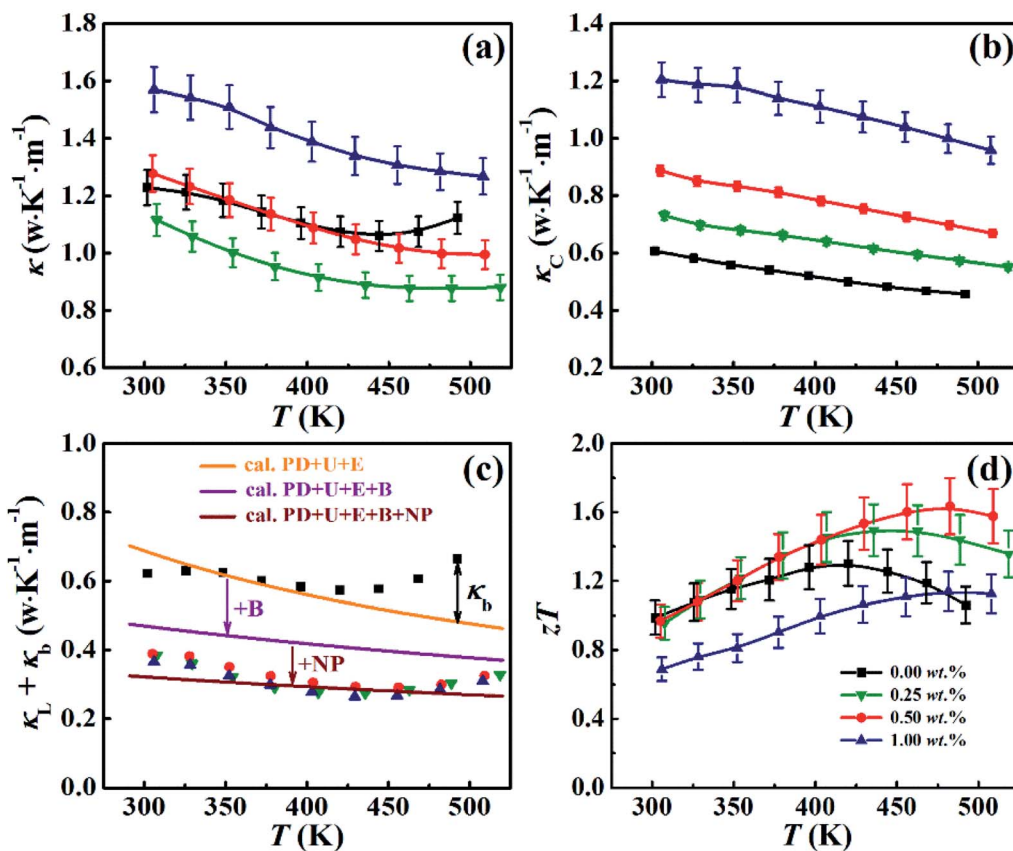


Fig. 5 Temperature dependences of (a) total thermal conductivity  $\kappa$ , (b) carrier thermal conductivity  $\kappa_c$ , (c) lattice thermal conductivity plus thermal conductivity from the bipolar effect  $\kappa_L + \kappa_b$ , and (d)  $ZT$  values for composite samples  $\chi$ (PbTe)/BST ( $\chi = 0, 0.25, 0.5$  and  $1.0$  wt%).

scattering from the interfaces (IF).  $A$ ,  $B$  and  $C$  are the pre-factors for the scattering from point defects (including embedded PbTe nanoparticles) (PD), Umklapp process ( $U$ ) and the electron-phonon interaction ( $E$ ), respectively. To calculate quantitatively  $\kappa_L$  through formula (4), the literature values of Debye temperature  $\theta_D = 94$  K for BST and average sound velocity  $v = 2147$  m s $^{-1}$  were used.<sup>34</sup> By substituting formula (6) for  $\tau_T$  in formula (4) and through fitting the experimental  $\kappa_L$  to formula (4), one can obtain calculated  $\kappa_L$  (solid orange line in Fig. 5(c)) and magnitudes for parameters  $A$  and  $B$  for the BST matrix (Table S2†). It can be seen that the calculated  $\kappa_L$  is fitting well with the experimental data of the BST matrix in the temperature range of 300–450 K. For the composite samples ( $\chi > 0$ ), only considering the additional scattering from the interfaces (IF), the calculated  $\kappa_L$  will decrease to the position of the solid purple line as shown in Fig. 5(c), manifested as the addition of  $v/l$  ( $l = 126$  nm as shown in Table S2†) in formula (6). Moreover, further considering the enhancement of phonon scattering by the PbTe nanoparticles (NP),  $\kappa_L$  will decrease to the position of the wine line (being manifested as the rise of  $A$  from 0.69 to  $1.41 \times 10^{-40}$  s $^3$  as shown in Table S2†), which is fitting well with the experimental data for the composite samples ( $\chi > 0$ ) as shown in Fig. 5(c). Consequently, the introduction of PbTe nanoparticles leads to a large reduction of  $\kappa_L$  for the composite samples.

Fig. 5(d) shows  $ZT$  for all the samples. Although the temperature behavior of  $ZT$  for all samples is similar: it increases with increasing temperature, and after reaching a maximum value  $ZT$  decreases with further increasing temperature, the peak temperatures (at which  $ZT$  gets a maximum value) for  $ZT$  of the composite samples ( $\chi > 0$ ) are larger than that of the BST matrix. Specially,  $ZT$  of the sample with  $\chi = 0.5$  wt% is larger than that of the BST matrix in almost the whole temperature range, and reaches a maximum value of  $ZT = 1.6$  at 482 K, which is  $\sim 25\%$  larger than that of the BST

Table 1  $ZT_{\max}$  and  $ZT_{\text{ave}}$  values at 300–500 K of BST matrix, (0.5 wt% PbTe)/BST composite sample and other reported state-of-the-art p-type BiSbTe-based alloys as well as typical TE materials

TE materials	$ZT_{\max}$	$ZT_{\text{ave}}$	Ref.
BiSbTe (ball milled nano-alloys)	1.4	1.3	12
CuGaTe <sub>2</sub> /BiSbTe	1.53	1.36	20
Bi <sub>0.5</sub> Sb <sub>1.495</sub> Cu <sub>0.005</sub> Te <sub>3</sub>	1.4	1.2	21
ZnTe/BiSbTe	1.4	1.2	22
Fe <sub>3</sub> O <sub>4</sub> /BiSbTe	1.5	1.25	23
$\alpha$ -MgAgSb	1.4	1.2	24
PbTe	0.78	0.37	16
SnSe	1.5	1.12	25
BST matrix	1.3	1.19	This work
PbTe/BST	1.6	1.38	This work

matrix ( $ZT_{\max} = 1.3$  at 420 K). Moreover, the sample with  $\chi = 0.5$  wt% exhibits the highest average  $ZT_{\text{ave}}$  of 1.38 in the temperature range from 300 to 500 K, with the average  $ZT^4$

$$ZT_{\text{ave}} = \frac{\int_{T_c}^{T_h} Z(T) dT}{\Delta T} \frac{T_h + T_c}{2} \quad (7)$$

where  $T_h$  and  $T_c$  are the hot side temperature and the cold side temperature, respectively. Both the  $ZT_{\max}$  and  $ZT_{\text{ave}}$  values of the composite sample with  $\chi = 0.5$  wt% are comparable to other reported state-of-the-art p-type BiSbTe-based alloys as well as typical TE materials,<sup>12,16,20-25</sup> as shown in Table 1.

## 4. Conclusions

In summary, the incorporation of small content (0.5 wt%) of PbTe nanoparticles into BST matrix can lead to excellent TE performance resulting from concurrent increase in PF and decrease in  $\kappa_L$ . The increase in PF is mainly benefited from the optimization of  $p$ , maintenance of  $\mu$  and constant rise in  $S$  due to inhibition of the transport of thermally excited electrons by the interface potentials; while by using the Callaway model we demonstrate that the ultralow  $\kappa_L$  of 0.26 W m<sup>-1</sup> K<sup>-1</sup> at 429 K for  $\chi(\text{PbTe})/\text{BST}$  ( $\chi = 0.5$  wt%) can be attributed to the enhanced phonon scattering by dispersed PbTe nanoparticles and the interfaces between the PbTe and BST matrix. As a result, a highest  $ZT_{\max}$  of 1.6 (at 482 K) and an average  $ZT_{\text{ave}}$  of 1.38 (at 300–500 K) are achieved in the composite system with 0.5 wt% of PbTe. Present study demonstrates that the thermoelectric performance of BST can be effectively improved by incorporating proper amount of PbTe nanophase.

## Author contributions

Yuanyue Li: conceptualization, data curation, funding acquisition, writing-original draft. Mengna Ren: formal analysis, software, visualization, investigation. Zhongsen Sun: resources, methodology, writing-review & editing. Zhao Yao: project administration, supervision, validation, writing-review & editing.

## Conflicts of interest

There are no conflicts to declare.

## Acknowledgements

Financial support from China Postdoctoral Science Foundation (No. 2017M612193), Natural Science Foundation of Shandong Province (No. ZR2018BEM017) and Qingdao Postdoctoral Applied Research Project Foundation is gratefully acknowledged.

## References

- 1 C. Yu and K. T. Chau, *Energy Convers. Manage.*, 2009, **50**, 1506–1512.
- 2 L. E. Bell, *Science*, 2008, **321**, 1457–1461.
- 3 T. Fujigaya, *Bull. Chem. Soc. Jpn.*, 2019, **92**, 400–408.
- 4 D. M. Rowe, *Thermoelectrics handbook: macro to nano*, CRC Press, 2005.
- 5 W. D. Liu, L. Yang, Z. G. Chen and J. Zou, *Adv. Mater.*, 2020, **32**, 1905703.
- 6 L. Yang, Z. G. Chen, M. S. Dargusch and J. Zou, *Adv. Energy Mater.*, 2018, **8**, 1701797.
- 7 C. Gayner and Y. Amouyal, *Adv. Funct. Mater.*, 2020, **30**, 1901789.
- 8 D. Li, R. R. Sun and X. Y. Qin, *Intermetallics*, 2011, **19**, 2002–2005.
- 9 ö. C. Yelgel and G. P. Srivastava, *J. Appl. Phys.*, 2013, **113**, 073709.
- 10 S. I. Kim, K. H. Lee, H. A. Mun, H. S. Kim, S. W. Hwang, J. W. Roh, D. J. Yang, W. H. Shin, X. S. Li, Y. H. Lee, G. J. Snyder and S. W. Kim, *Science*, 2015, **348**, 109–114.
- 11 J. Pei, B. W. Cai, H. L. Zhuang and J. F. Li, *Natl. Sci. Rev.*, 2020, **7**, 1856–1858.
- 12 B. Poudel, Q. Hao, Y. Ma, Y. C. Lan, A. Minnich, B. Yu, X. Yan, D. Z. Wang, A. Muto, D. Vashaei, X. Y. Chen, J. M. Liu, M. S. Dresselhaus, G. Chen and Z. F. Ren, *Science*, 2008, **320**, 634–638.
- 13 S. F. Fan, J. N. Zhao, J. Guo, Q. Y. Yan, J. Ma and H. H. Hng, *Appl. Phys. Lett.*, 2010, **96**, 182104.
- 14 J. H. Li, Q. Tan, J. F. Li, D. W. Liu, F. Li, Z. Y. Li, M. M. Zou and K. Wang, *Adv. Funct. Mater.*, 2013, **23**, 4317–4323.
- 15 Y. C. Dou, X. Y. Qin, D. Li, L. L. Li, T. H. Zou and Q. Q. Wang, *J. Appl. Phys.*, 2013, **114**, 044906.
- 16 K. Biswas, J. H. He, I. D. Blum, C. I. Wu, T. P. Hogan, D. N. Seidman, V. P. Dravid and M. G. Kanatzidis, *Nature*, 2012, **489**, 414–418.
- 17 G. J. Tan, F. Y. Shi, S. Q. Hao, L. D. Zhao, H. Chi, X. M. Zhang, C. Uher, C. Wolverton, V. P. Dravid and M. G. Kanatzidis, *Nat. Commun.*, 2016, **7**, 12167.
- 18 S. J. Liang, J. T. Xu, H. X. Wang, X. J. Tan, G. Q. Liu, H. Z. Shao, B. Yu, S. Yue and J. Jiang, *J. Mater. Sci.: Mater. Electron.*, 2018, **29**, 7701–7706.
- 19 B. Xu, M. T. Agne, T. L. Feng, T. C. Chasapis, X. L. Ruan, Y. L. Zhou, H. M. Zheng, J. H. Bahk, M. G. Kanatzidis, G. J. Snyder and Y. Wu, *Adv. Mater.*, 2017, **29**, 1605140.
- 20 Y. Y. Li, X. C. Wang, G. X. Liu, B. C. Shin and F. K. Shan, *Scr. Mater.*, 2019, **172**, 88–92.
- 21 F. Hao, P. F. Qiu, Y. S. Tang, S. Q. Bai, T. Xing, H. S. Chu, Q. H. Zhang, P. Lu, T. S. Zhang, D. D. Ren, J. K. Chen, X. Shi and L. D. Chen, *Energy Environ. Sci.*, 2016, **9**, 3120–3127.
- 22 R. G. Deng, X. L. Su, S. Q. Hao, Z. Zheng, M. Zhang, H. Y. Xie, W. Liu, Y. G. Yan, C. Wolverton, C. Uher, M. G. Kanatzidis and X. F. Tang, *Energy Environ. Sci.*, 2018, **11**, 1520–1535.
- 23 C. C. Li, S. F. Ma, P. Wei, W. T. Zhu, X. L. Nie, X. H. Sang, Z. G. Sun, Q. J. Zhang and W. Y. Zhao, *Energy Environ. Sci.*, 2020, **13**, 535–544.
- 24 D. D. Li, H. Z. Zhao, S. M. Li, B. P. Wei, J. Shuai, C. L. Shi, X. K. Xi, P. J. Sun, S. Meng, L. Gu, Z. F. Ren and X. L. Chen, *Adv. Funct. Mater.*, 2015, **25**, 6478–6488.



25 L. D. Zhao, G. J. Tan, S. Q. Hao, J. Q. He, Y. L. Pei, H. Chi, H. Wang, S. K. Gong, H. B. Xu, V. P. Dravid, C. Uher and G. J. Snyder, *Science*, 2016, **351**, 141–144.

26 Y. Y. Li, D. Li, X. Y. Qin, X. H. Yang, Y. F. Liu, J. Zhang, Y. C. Dou, C. J. Song and H. X. Xin, *J. Mater. Chem. C*, 2015, **3**, 7045–7052.

27 Y. Y. Li, X. Y. Qin, D. Li, J. Zhang, C. Li, Y. F. Liu, C. J. Song, H. X. Xin and H. F. Guo, *Appl. Phys. Lett.*, 2016, **108**, 062104.

28 Z. M. Gibbs, H. S. Kim, H. Wang and G. J. Snyder, *Appl. Phys. Lett.*, 2015, **106**, 022112.

29 T. H. Zou, X. Y. Qin, D. Li, G. L. Sun, Y. C. Dou, Q. Q. Wang, B. J. Ren, J. Zhang, H. X. Xin and Y. Y. Li, *Appl. Phys. Lett.*, 2014, **104**, 013904.

30 S. K. Li, X. R. Liu, Y. D. Liu, F. S. Liu, J. Luo and F. Pan, *Nano Energy*, 2017, **39**, 297–305.

31 E. S. Toberer, P. Rauwel, S. Gariel, J. Taftø and G. J. Snyder, *J. Mater. Chem.*, 2010, **20**, 9877–9885.

32 J. Callaway, *Phys. Rev.*, 1959, **113**, 1046–1051.

33 W. Kim, J. Zide, A. Gossard, D. Klenov, S. Stemmer, A. Shakouri and A. Majumdar, *Phys. Rev. Lett.*, 2006, **96**, 045901.

34 H. S. Kim, S. I. Kim, K. H. Lee, S. W. Kim and G. J. Snyder, *Phys. Status Solidi B*, 2017, **254**, 1600103.

